RESEARCH PAPER

Effect of biochar on the photocatalytic activity of nitrogen-doped titanium dioxide nanocomposite in the removal of aqueous organic pollutants under visible light illumination

Hassan Hosseini-Monfared [1*], Yasaman Mohammadi [2], Reza Montazeri [2], Sakineh Gasemzadeh [2], Rajender S. Varma [3]

[1] Department of Chemistry, Amirkabir University of Technology, Tehran, Iran.

[2] Department of Chemistry, University of Zanjan, Zanjan, Iran.

[3] Regional Centre of Advanced Technologies and Materials, Czech Advanced Technology and Research Institute, Palacky University, Šlechtitelů 27, 783 71 Olomouc, Czech Republic

ARTICLE INFO

Article History:
Received 15 December 2020
Accepted 18 Februar 2021
Published 15 March 2021

Keywords:
Biocarbon
TiO_2
Doping
Oxygen vacancy
Photocatalysis

ABSTRACT

Biochar, as a low-cost carbon obtained from barley straw, was used for the simple sol–gel synthesis of visible-light photocatalysts comprising N-doped TiO_2/biochar nanocomposite (N-TiO_2/C) and thermally treated N-TiO_2/C. The nanocomposites were characterized by SEM, EDX, TEM, XRD, BET, FTIR, DRS UV-vis, and PL measurements. The doped TiO_2 catalyzed the photodegradation of rhodamine B (RhB) in aqueous dispersion under visible-light illumination where the N-TiO_2/C nanocomposite with a band-gap of 2.96 eV and large surface area (206 m^2 g^{-1}) demonstrated the highest photocatalytic activity and degrading 99% of RhB under visible light of a 40-Watt white LED lamp within 105 min. Photoluminescence (PL) spectroscopy experiments revealed the effective separation of charge carriers by the N-doped TiO_2 materials. The presence of carbon enhances the photocatalytic activity of N-TiO_2 material by decreasing the band gap, enhancing the visible light absorption, reducing the reflection of light, enhancing the adsorption of RhB and intermediates on the N-TiO_2 surface, thus prolonging the separation electrons (e^-) and valence band hole (h^+).

How to cite this article
Hosseini-Monfared H., Mohammadi Y., Montazeri R., Gasemzadeh S., Varma R.S. Effect of biochar on the photocatalytic activity of nitrogen-doped titanium dioxide nanocomposite in the removal of aqueous organic pollutants under visible light illumination. Nanochem Res, 2021; 6(1):79-93. DOI: 10.22036/ncr.2021.01.008

INTRODUCTION

Dyes are of the principal pollutants of water because of their high chemical oxygen demand (COD) and extensive absorption of visible light radiation [1]. The resulting water pollution leads to a global decrease in the availability of clean and safe water from available resources. The photocatalytic strategy is an effective and cleaner option for treating the organically polluted water bodies [2]. The degradation of organic dyes using light and semiconductors occurs through a photocatalytic or photo-assisted (photosensitized) oxidation mechanism depending on the process of charge carrier generation [3]. The photocatalytic purification of dye wastewater by irradiated TiO_2 has proven its effectiveness due to the high efficiency, stability, and relative non-toxicity of TiO_2 [4]. However, the practical application of TiO_2 alone, while using solar energy, is hindered by its low adsorption ability and the essential requirement of exclusive UV radiation for its surface photoactivation primarily due to a large optical band gap (E_g = 3.2 eV). Additional drawbacks of TiO_2 materials are limited quantum yields because of high recombination rates of

* Corresponding Author Email: *hahomonfared@gmail.com*

photon-induced electron-hole pairs that lead to limited applications under solar light [5] and weak separation efficiency of photocarriers, which results in low photocatalytic activity.

Doping is an effective method to extend the light absorption and photoactivation of TiO_2 to the visible light region and enhancing the utilization efficiency of solar energy [6]. Nitrogen doping is by far the most studied system and an ideal option for the preparation of visible-light responsive TiO_2 [6-8]. Zhu et al. prepared *N*-doped TiO_2 nanofibers with a shell of TiO_2 anatase [9]; higher photocatalytic activity under visible-light irradiation was related to the effective adsorption of organic molecule and the activation of O_2 by the surface layer. Sakthivel et al. synthesized the *N*-TiO_2 photocatalysts and used them for the mineralization of 4-chlorophenol under visible light [10].

Kamat et al. reported on the photodegradation of dyes pre-adsorbed on the surface of TiO_2 particles under visible light [11]; only the molecules that were in direct contact with the TiO_2 surface underwent photodegradation. Zhang et al. studied the decomposition of dyes in an aqueous TiO_2 dispersion under irradiation by visible light [12] where the dyes adsorbed on the surface of TiO_2 particles act as sensitizer and inject electrons into the conduction band of TiO_2 from their respective excited states and promote self-photosensitized decomposition [13]. Chung et al. synthesized *N*- and *S*-codoped TiO_2 (NS-TiO_2) and studied their visible light photocatalytic activity [14]; post thermal treatment of NS-TiO_2 decreased the photocatalytic activity. In addition, carbon modified TiO_2 can indeed improve the visible light photocatalytic activity [15] where carbon species serve a surface sensitizer and improve the visible light activity of carbon-modified TiO_2 [16]. Furthermore, Wang et al. showed that nanosized carbon on the surface of TiO_2/carbon composite improves the separation of photogenerated electrons and holes by capturing the electrons, which sensitizes TiO_2 for the absorption of more light on the catalyst surface [17].

Biochar is a carbon material prepared via the pyrolysis of plant and animal-based biomass under an inert atmosphere [18] and comprises abundant oxygen functional groups, an aromatic surface, a large surface area endowed with high porosity [19]. Owing to its high specific surface area and rich functional groups [20], biochar is an excellent sorbent to remove organic pollutants from aqueous solutions. Cai et al. developed composites made up of supported TiO_2 on biochar and used them as adsorptive photocatalyst for degradation of organic pollutants [21]. Acid pre-treated biochar (pBC) has been used as a support for TiO_2 to fabricate photocatalyst, TiO_2/pBC [22]. Kim et al. studied photocatalyst TiO_2 supported on biochar for the degradation of sulfamethoxazole [23]. TiO_2-coated biochar composites were also deployed for the removal of safranine T [21]. The results have demonstrated that loading of TiO_2 enhanced the adsorption ability of biochar and the high specific surface area of the biochar synergistically promoted the photocatalytic activity of TiO_2.

In this study, nitrogen-doped TiO_2/carbon nanocomposite is developed to obtain a highly active and visible-light photocatalyst that benefits from the *N*-doping effect, cooperative adsorption, and sensitization performance of biochar.

MATERIALS AND METHODS

Materials

Titanium (IV) isopropoxide ($Ti(OCH(CH_3)_2)_4$, TTIP) as the TiO_2 precursor, rhodamine B (tetraethylrhodamine, RhB), acetylacetone, urea, absolute ethanol and other chemicals were of analytical reagent grade purchased from Merck and were used without further purification. Deionized (DI) water was used for all the experiments. The TiO_2 (P25) sample by Degussa was used as reference, a nonporous powder material comprising a mixture of anatase and rutile (80:20) with a BET surface area of about 50 $m^2\ g^{-1}$ and an average particle size of about 30 nm [24].

UV–vis spectra of the solutions were run on an Analytik Jena Specord 210 Plus Spectrophotometer. Photoluminescence emissions were recorded on a LS 55 Perkin Elmer Fluorescence Spectrometer. Fourier transform infrared (FTIR) spectra were taken using a Thermo Scientific Nicolet iS10 FTIR Spectrometer. Powder X-ray diffraction patterns were collected at a X'Pert Pro Company, wavelength 1.5406 Å (Cu Kα), voltage 40 kV, current 40 mA. The average crystallite size ($D_{Scherrer}$) was calculated by the Scherrer equation Eq. (1) [25]:

$$D_{Scherrer} = k\lambda / (\beta . \cos \theta) \quad (1)$$

where k is the shape factor; λ represents the x-ray wavelength used for the measurement; β is the line width (FWHM) in radians, and θ is the Bragg angle. Scanning electron microscopy-

energy dispersive X-ray spectroscopy (SEM-EDX) were taken using a FEI QUANTA200 ESEM. Transmission electron microscopic (TEM) images were generated by an EM 208S electron microscope. N_2 adsorption (Belsorp-mini, Japan) was used for determining the surface area (Brunauer-Emmett-Teller (BET) method), and N_2 desorption was used for the estimation of pore volume and pore size distribution (Barrett-Joyner-Halenda (BJH) method). Light absorptions in UV and visible ranges were studied by UV-visible diffuse reflectance spectroscopy (UV-vis DRS; *AvaSpec-ULS2048LTEC*). Band gap energies of the photocatalysts were estimated from the plots of light absorptions using Tauc's equation(Equation 2) [26]:

$$a(h\nu) = B(h\nu - E_g)^n \quad (2)$$

where B is a constant; α is molar extinction coefficient; $h\nu$ is photon energy; E_g is average energy gap; and n is ½ for allowed direct transition (plotted as $a(h\nu)^2$ versus E).

Synthesis and treatment of biochar

The barley straw was used as the biomass obtained from farms in the city of Zanjan, Zanjan Province, Iran. The barley straw was dried at room temperature and then milled to pass a 0.50 mm size screen. The milled barley straw was first dewaxed in a Soxhlet apparatus using ethanol 96% and dried at 55 °C for 24 h. Then, it was pyrolyzed at 500 °C under a nitrogen flow at 60 sccm in a tubular furnace for 2 h with the heating rate of 5 °C min^{-1}. The obtained biochar was cooled and washed at least three times with DI water. This was followed by drying at 80 °C for 24 h.

For acid treatment, 0.10 g of the obtained dried biochar was dispersed in 15 mL of 65% HNO_3 and refluxed at 80 °C for 1 h. The ensuing treated biochar was separated by centrifugation and washed with DI water until the pH of the filtrate reached 7. Finally, it was oven-dried at 105 °C for 12 h.

Preparation of nitrogen doped TiO_2 (N-TiO_2)

Doped TiO_2 hybrid material was prepared using the sol-gel method. As a dopant source, 3.3 mmol (0.2 g, 60.06 g/mol) of urea was dissolved in 12 mL of absolute ethanol. It was added to 3.4 mmol of titanium (IV) isopropoxide (TTIP) and 7.8 mmol of acetylacetone dissolved in 5 mL of absolute ethanol under vigorous stirring, followed by adding deionized water (0.4 mL). After 10 minutes, the solution was transferred to a 25 mL Teflon lined stainless-steel autoclave, and the solvothermal treatment was performed at 115 °C for 12 h. The resulting cream-color powder was washed several times with deionized water and methanol by centrifugation. The washed sample was dried at 60 °C for 24 h.

Synthesis of nitrogen doped TiO_2/carbon nanocomposite (N-TiO_2/C)

A mixture of 0.02 g of acid treated biochar and 3.3 mmol of urea in 12 mL of absolute ethanol was prepared and sonicated using an ultrasound bath for 30 min. It was added to 3.4 mmol of TTIP and 7.8 mmol of acetylacetone in 5 mL of absolute ethanol under vigorous stirring. It was followed by the addition of 0.40 mL of deionized water and the stirring continued for additional 10 minutes. The mixture was transferred to a 25 mL Teflon lined stainless-steel autoclave and aged at 115 °C for 12 h. The resulting brown solid was dried at 70 °C for 12 h. Then it was washed several times with deionized water and methanol and dried at 60 °C for 24 h to get the N-TiO_2/C sample.

The dried N-TiO_2/C gel was subsequently ground into a fine powder and calcined at 500 °C with the rate of 5 °C min^{-1} under N_2 for 2 h to yield the gray N-TiO_2/C(500).

Photoreactor and light source

A 40-Watt white LED lamp was positioned at 5 cm above a thermostated Pyrex cylindrical double-walled reactor which was placed in a black wooden box. The temperature of the photocatalytic reaction was maintained at 25 °C by water circulation.

Photocatalytic properties of the samples

For photocatalytic activity evaluations, the photodegradation of RhB was studied as a model compound because it is a common hazardous contaminant present in industrial wastewater [27]. An aqueous TiO_2 dispersion was prepared by adding 40 mg of photocatalyst (TiO_2, *N*-TiO_2 or *N*-TiO_2/C) powder to a 40 mL solution containing the RhB at 10 ppm concentration. Prior to irradiation, the dispersions were magnetically stirred in the dark for 30 min to secure the establishment of an adsorption/desorption equilibrium of RhB on the photocatalyst surface. At given irradiation time intervals, the dispersion was sampled (1 mL),

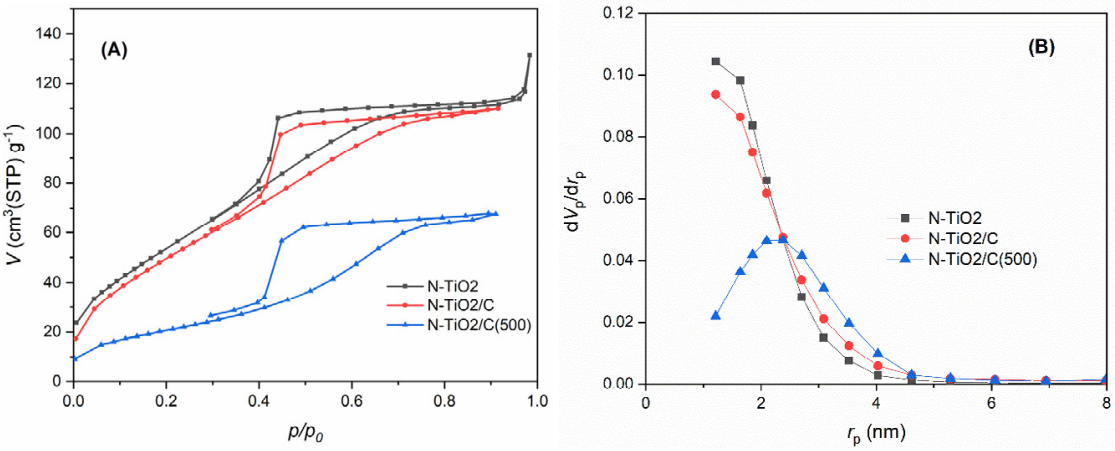

Fig. 1. (A) Nitrogen adsorption-desorption isotherm and (B) BJH plots of N-TiO_2, N-TiO_2/C and N-TiO_2/C(500) photocatalysts

Table 1. BET surface area and pore characteristics of the doped TiO_2 materials

Photocatalyst	BET surface area (m^2g^{-1})	Pore volume ($cm^3 g^{-1}$)	Pore diameter (BJH)[a] (nm)	S_{meso} (m^2g^{-1})
N-TiO_2	220	0.16	1.21	80
N-TiO_2/C	206	0.16	1.21	98
N-TiO_2/C(500)	80	0.09	2.38	23

[a] Obtained from the adsorption branch of nitrogen isotherm by the BJH method

diluted to 3 mL by DI water, centrifuged to separate the photocatalyst particles and UV-vis spectra of the supernatant (measured over the range of 200-800 nm) were recorded using an Analytik Jena Specord 210 Plus Spectrophotometer. All the photodegradation performances were assessed under visible light.

RESULTS AND DISCUSSION

Nitrogen-doped TiO_2 catalysts were successfully synthesized by an easy and low-cost one-step solvothermal method. In the preparation of *N*-TiO_2/C nanocomposite, biochar is probably grafted onto the surface of TiO_2 via C–O–Ti bonds under mild solvothermal synthesis conditions (115 °C for 12 h). This structure is suitable for the charge transfer upon light excitation [28]. A very high temperature (> 800 °C) is required for the synthesis of carbon-doped TiO_2, wherein carbon substitutes for some of the lattice oxygen atoms [29]. *N*-TiO_2/C nanocomposite prepared via this direct solvothermal synthesis is significantly brown, showing an electronic interaction and different bonding in this highly interpenetrated material than that of a gray colored physical mixture of carbon and TiO_2. Toward a better understanding of the influence of carbon, *N*-TiO_2 without carbon was also prepared. Notably, the results obtained by *N*-TiO_2 and *N*-TiO_2/C hybrid compounds demonstrated a significant effect of carbon on textural properties. In order to study the effect of heat treatment on the photocatalytic activity of *N*-TiO_2/C, it was calcinated at 500 °C.

Surface properties

The N_2 sorption isotherms and the corresponding BJH pore size distribution curves of the prepared nitrogen-doped TiO_2 samples are depicted in Fig. 1 (A) and 1 (B), respectively. As displayed in Fig. 1, the nitrogen isotherms of *N*-TiO_2, *N*-TiO_2/C and *N*-TiO_2/C(500) indicate the presence of mesoporous materials [30]. According to IUPAC classification [31], these doped materials exhibit isotherms type IV and their hysteresis are of triangular shape that is classified as H2 loops, indicating that the prepared composites have mesoporous structure with ink-bottle like pores [31].

The surface properties of the synthesized materials are summarized in Table 1. The most significant increase in the BET area is for *N*-TiO_2 compared to TiO_2. The surface area and pore

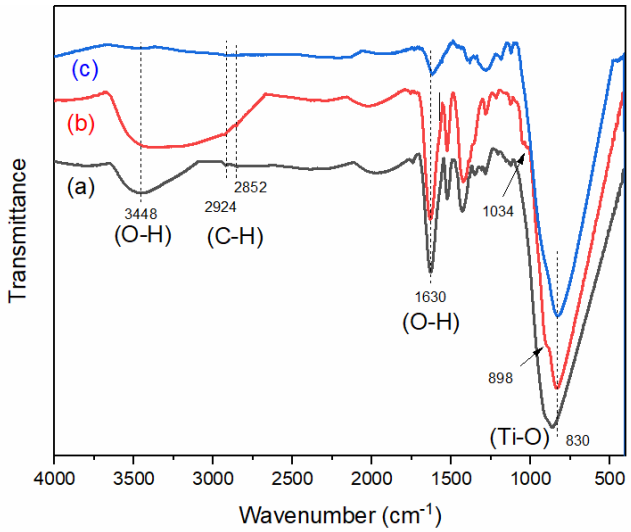

Fig. 2. FTIR spectra of (a) *N*-TiO_2, (b) *N*-TiO_2/C, and (c) *N*-TiO_2/C(500) materials.

volume of N–TiO_2 were determined to be 220 m^2 g^{-1} and 0.16 cm^3 g^{-1}, respectively. The BET specific surface area of titania increased with the N-doping due to the suppression of the TiO_2 crystal growth by urea. Although the surface area of *N*–TiO_2 was decreased to some extent by the addition of treated biochar, it is approximately four times higher than that of TiO_2. The specific surface area (from 206 m^2 g^{-1} to 80 m^2 g^{-1}) and pore volume (from 0.16 cm^3g^{-1} to 0.09 cm^3g^{-1}) decreased with the calcination of *N*-TiO_2/C due to the sintering and crystal growth of TiO_2 particles. Correspondingly, the pore diameter of *N*-TiO_2/C(500) material increased from 1.21 nm to 2.38 nm (Table 1). The pore volume (0.16 cm^3 g^{-1}) and pore diameter (1.21 nm) of *N*-TiO_2 and *N*-TiO_2/C are the same. These findings are consistent with our previous statements that TiO_2 is not doped with carbon in *N*-TiO_2/C material.

For the synthesized materials the mesopore surface area (S_{meso} (m^2 g^{-1})) was equal to the difference between the total surface area (S_{BET}) and the slop of t-plot that shows mesoporous plus external surface area (Table 1) [32]; *N*-TiO_2/C nanocomposite exhibited the highest mesoporous surface area (98 m^2g^{-1}) that would provide more opportunities for the interaction of reactants with active sites of the photocatalyst, thus leading to greater activities. As expected, the comparison of *N*-TiO_2 with *N*-TiO_2/C shows that the mesopore surface area was increased by the presence of biochar from 80 m^2 g^{-1} to 98 m^2 g^{-1}. The most noticeable point is the decrease of mesoporous surface area from 98 m^2 g^{-1} for *N*-TiO_2/C to 23 m^2 g^{-1} in *N*-TiO_2/C(500) upon calcination due to the carbon degradation during calcination at 500 °C (Table 1). The high surface area and porosity of *N*-TiO_2/C material is indicative of a larger number of photocatalytic surface-active centers and the adsorption sites for compounds, with enhanced ease of reactants' transport through the mesopores.

FTIR spectroscopy

Fig. 2 shows the spectra of nitrogen doped TiO_2 samples in the range of 400–4000 cm^{-1}. The strong and very broad peaks in the region 500-1080 cm^{-1} can be considered as the stretching vibration of Ti-O and Ti–O-Ti bonds [33] combined with the stretching vibration of Ti–O–C bonds [34]. *N*-TiO_2 and *N*-TiO_2/C show a very broad peak at about 3448 cm^{-1} that is assigned to the stretching vibration of adsorbed water and hydroxyls on the surface of TiO_2, and the peak appearing at 1630 cm^{-1} is attributed to the bending vibration of the O–H bond in hydroxyls and adsorbed water (Fig. 2(a) and (b)) [35]. In comparison to *N*-TiO_2, the band for *N*-TiO_2/C nanocomposite span remarkably over a wider range from 3675 to 2672 cm^{-1}, suggesting that the *N*-TiO_2/C surface is richer than *N*-TiO_2 in hydroxyl groups, which can be a piece of evidence for the existence of higher Ti–OH [36]. For this reason, H_2O is more easily adsorbed on the surface of this biochar modified nanocomposite. The hydroxyl groups present on the surface directly generate OH radical when reacted with the photogenerated

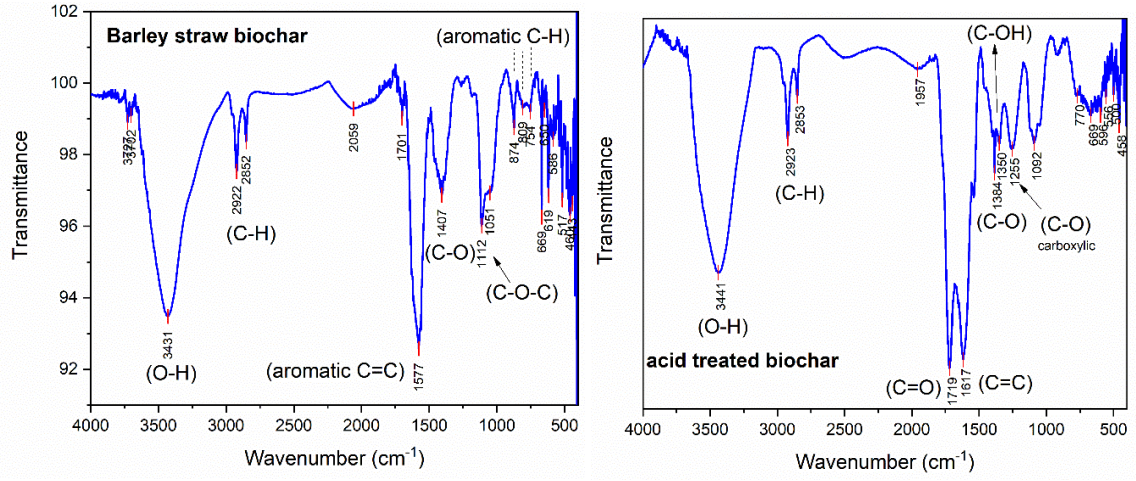

Fig. 3. The FTIR spectra of biochar and acid treated biochar.

hole during the photocatalysis. As adsorbed water and hydroxyls play an important role in the photocatalytic activity [37], the strong intensity of the peak at 1630 cm^{-1} indicates a high content of adsorbed water and hydroxyls in the sample, which is helpful for enhancing the photocatalytic activity of *N*–TiO_2/C. It has been shown that hydrogen-bonding interactions between adsorbed water and TiO_2 stabilize photogenerated charge carriers (e^- and h^+) in nanocrystalline TiO_2 and suppress their recombination [35]. The peaks at 1527 cm^{-1} and 1421 cm^{-1} are from the impurities, probably acetyl acetonate, that has not been completely removed in the wash. It can be observed that the intensities of absorption bands of adsorbed water and oxygen-containing functional groups such as C-O and Ti-OH (3448, 1630, 1527 and 1421 cm^{-1}) were dramatically reduced during the calcination at 500 °C in *N*-TiO_2/C(500), Fig. 2(c). The presence of a small peak at 1034 cm^{-1} in the spectrum of *N*-TiO_2/C was attributed to the C-H stretching vibration from the unreacted precursor TTIP reflects the incomplete substitution with OH groups of H_2O. The bands observed at 2960, 2924, and 2849 cm^{-1} are also assigned to the C-H stretching vibration of organic species remaining on the sample surface.

For comparison, the FTIR spectra of biochar and acid treated biochar are shown in Fig. 3.

SEM and TEM analyses

The morphology and microstructure of the prepared *N*-TiO_2/C were probed with SEM (see Fig. 4). It could be observed that the *N*-TiO_2/C particles are spherical with an uneven distribution of agglomerated particles. EDX analysis showed that *N*-TiO_2/C consists of 0.21 wt% doped nitrogen and 3.05 wt% carbon (Fig. 4). The Ti and O content in *N*-TiO_2/C were 60.97 wt% and 35.76 wt%, respectively, the molar Ti:O ratio being 1:1.76 (33.69:59.17). It is evident that the nanocomposite is, in fact, a non-stoichiometric compound with surface oxygen vacancies and the formula of *N*-TiO_{2-x}/C. It is usual that *N*-doping and the formation of oxygen vacancies and electrons occur together to support the neutrality of the lattice. It has been proven [38] that two adjacent Ti atoms of the removed oxygen atom are reduced to Ti^{3+}. As a result, donor states about 0.75–1.18 eV below the conduction band edge ensued [39]. The coupling of *N*-doping with the formation of oxygen vacancies prevent the recombination of the photogenerated e^-/h^+ recombination as well as enhance the visible light absorbance [40]. Additionally, the obtained and coordinatively unsaturated Ti species may act as catalytic sites [38]. Interestingly, the presence of surface Ti^{3+} defects can also enhance the photocatalytic performance by increasing the oxygen adsorption in conjunction with trapping the photogenerated electrons, which prevents the electron-hole recombination [41].

Studies of the *N*-TiO_2/C nanocomposite by TEM showed that it is composed of irregular sphere-like nanoparticles with uniform distribution and size 3-10 nm, Fig. 5. The small size and uniform distribution of particles may be favorable for the adsorption and photoreactions.

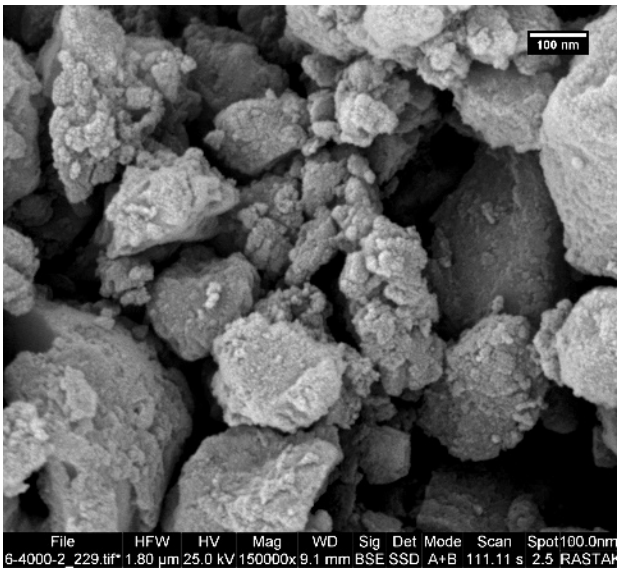

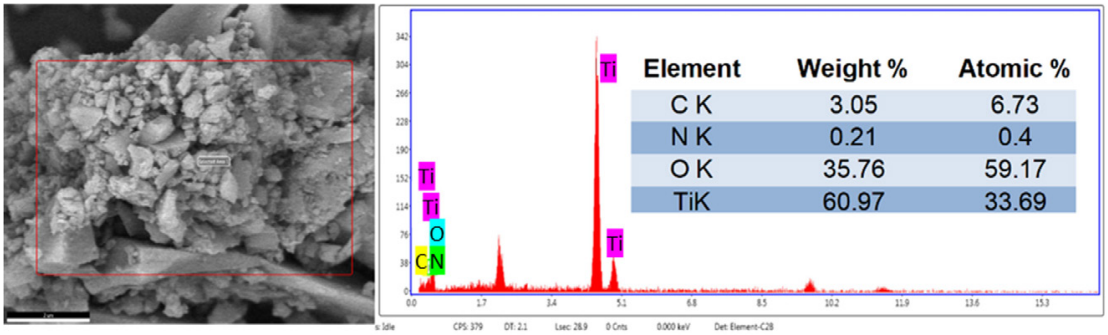

Fig. 4. SEM image and EDX analysis of the *N*-TiO_2/C nanocomposite.

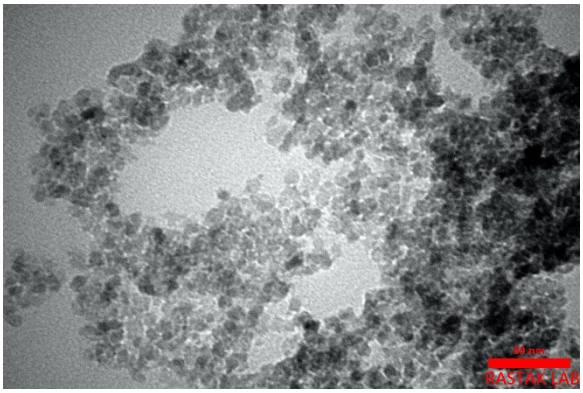

Fig. 5. TEM image of N-TiO_2/C; scale bar 50 nm

XRD characterization

XRD patterns displayed in Fig. 6 pointed out the clear presence of a distinctive anatase phase in *N*-TiO_2/C and *N*-TiO_2/C(500) samples. In terms of the rates of recombination e^-/h^+ and adsorptive affinity for organic compounds, TiO_2 anatase phase goes beyond TiO_2 rutile phase [42]. There are no peaks for the dopant N and modifier C due to their

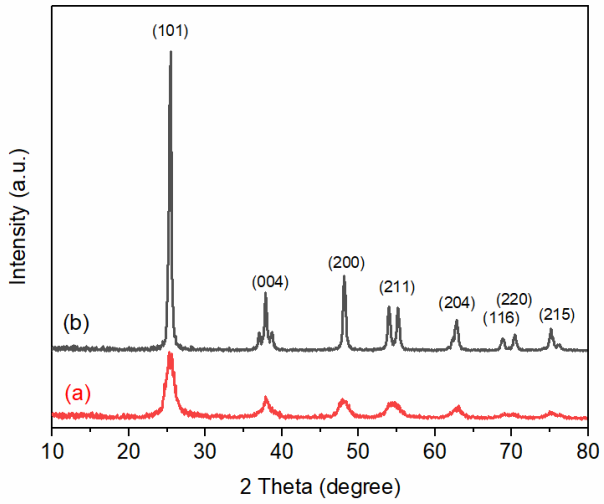

Fig. 6. X-ray diffraction (XRD) pattern of (a) N-TiO_2/C and (b) N-TiO_2/C(500)

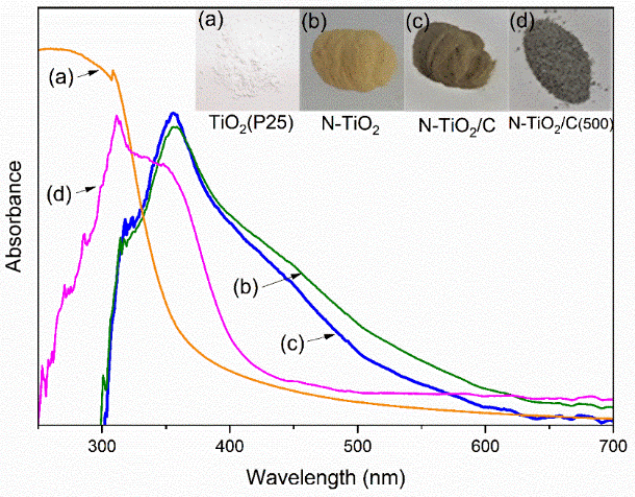

Fig. 7. Diffuse reflectance UV-visible absorption spectra of *N*-TiO_2, *N*-TiO_2/C, *N*-TiO_2/C(500) and pure TiO_2; inset photos show the samples colors which reflect the band gap energies

low weight percent in the doped TiO_2. Without changing the anatase crystal phase, both materials exhibited almost identical XRD patterns differing only in terms of the intensity of the anatase diffraction lines. The diffraction peaks of *N*-TiO_2/C became sharper and their intensity increased via calcination in *N*-TiO_2/C(500). Meanwhile, the average crystallite size, calculated by the Scherrer method[25], increased with the calcination temperature from 10.3 nm for *N*-TiO_2/C to 33.1 nm in *N*-TiO_2/C(500).

Optical properties

Fig. 7 depicts the UV–vis absorption spectra for the prepared yellow-cream *N*-TiO_2, brown *N*-TiO_2/C, gray *N*-TiO_2/C(500) and white TiO_2. Following the introduction of nitrogen, both the *N*-TiO_2 and *N*-TiO_2/C demonstrate a noticeable red shift in the absorption band and a wide background absorption in the visible light region compared to TiO_2, which is a characteristic pattern of visible-light responsiveness. However, the TiO_2 sample responded only to the light of wavelengths shorter than 400 nm (Fig. 7(a)). Although the band gap energies of *N*-TiO_2 and *N*-TiO_2/C are not so low, their absorbances are not decreased rapidly as for TiO_2; they show a continuous curve until their absorbance reached zero at about 650 nm (Fig. 7(b) and (c)).

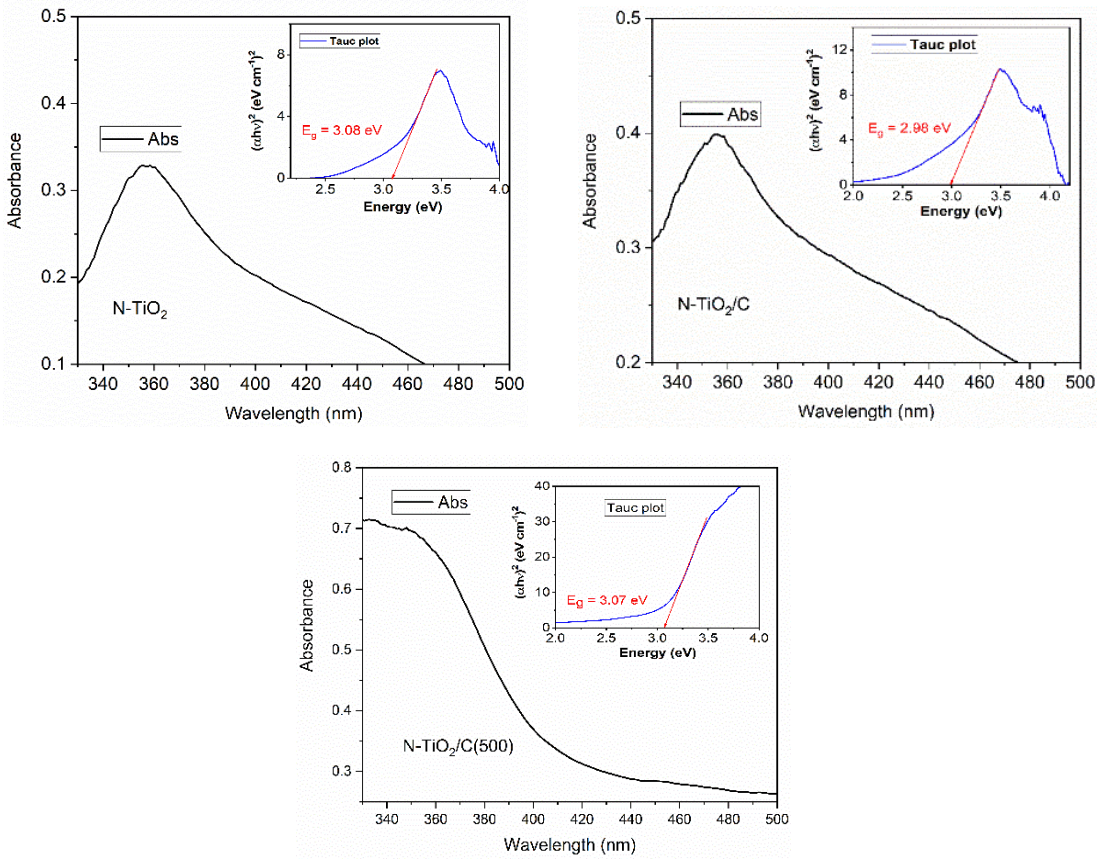

Fig. 8. Diffuse reflectance UV-visible spectra of *N*-TiO_2, *N*-TiO_2/C and *N*-TiO_2/C(500); inset diagrams show the Tauc plot and band gap calculation.

The continuous absorbance spectra for *N*-TiO_2 and *N*-TiO_2/C suggest a broad size distribution of the anatase nanocrystals. Various band gap is the result of a broad crystal size distribution, since the band gap energy of nanosized TiO_2 particles is strongly dependent on the crystal size [43]. Therefore, the long-ranged continuous visible-light absorbance spectrum of the *N*-TiO_2 and *N*-TiO_2/C results from the overlap between various absorbance spectra of nanocrystals. Accordingly, the wide background visible-light absorbances of *N*-TiO_2 and *N*-TiO_2/C show that these are efficient visible light-active photocatalysts. The band in the region below 400 nm is ascribed to the charge transfer process from O^{2-} (valence band) to Ti^{4+} (conduction band) under UV illumination [44]. The *N*-doping results in visible-light responsive photocatalyst by narrowing the band gap [45]. Additionally, it can be observed that the visible light background absorption of *N*-TiO_2/C sample is higher than that of *N*-TiO_2 due to the biochar effect as it can absorb visible light and prevent the reflection of light [17, 46]. Fig. 7(d) shows that after calcination at 550 °C, the composite *N*-TiO_2/C(500) displayed almost the same absorption band but the background visible-light absorption decreased. All these findings confirm that carbon species are modified on the surface of the *N*-TiO_2/C photocatalyst, forming the nanocomposite. Bonds such as Ti–O–C and Ti–OCO can be formed on the surface of TiO_2 by the biochar layer [17]. The close contact between the biochar carbon and *N*–TiO_2 facilitates the charge separation by trapping the photo-generated electrons [47]. The biochar species on the surface of the *N*-TiO_2/C sample serve as a surface sensitizer and enhances its visible-light photocatalytic activity by harvesting more visible light and the separation of photogenerated e^-/h^+ [48].

The Kubelka-Munk function was used to calculate the band gap by extrapolating the linear portion of the Tauc plot (Fig. 8). The band gap for *N*-TiO_2, *N*-TiO_2/C and *N*-TiO_2/C(500) were found to be 3.08, 2.98 and 3.07 eV, respectively, which are lower than that of commercial TiO_2, ~ 3.20 eV

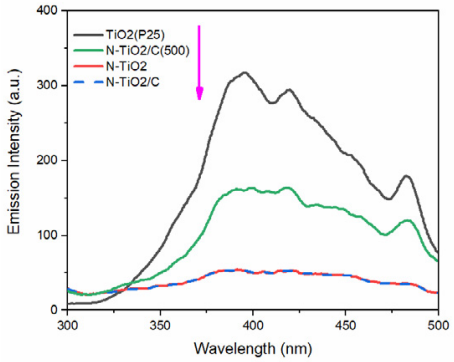

Fig. 9. Photoluminescence spectra of TiO_2, *N*-TiO_2, *N*-TiO_2/C, and *N*-TiO_2/C(500) materials dispersed in water with excitation wavelength of 270 nm

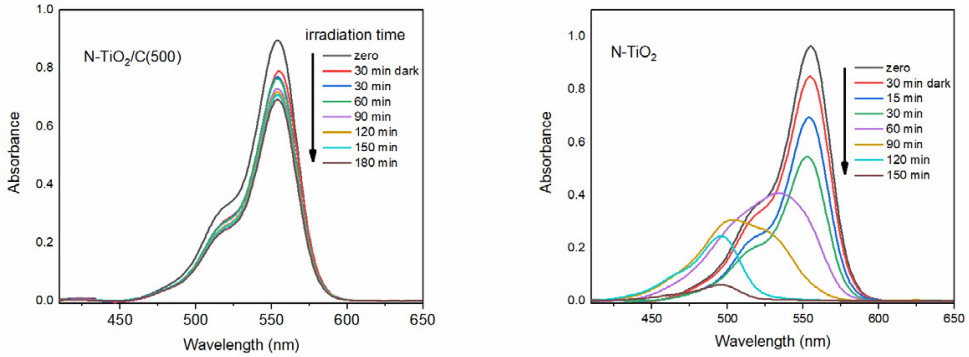

Fig. 10. UV-Vis spectral changes of a RhB solution under visible light irradiation and in the presence of *N*-TiO_2, (B) and *N*-TiO_2/C(500).

[26]. The *N*-TiO_2/C showed the lowest band gap energy and the highest visible light absorbance among the nitrogen-doped TiO_2 materials. In the case of *N*-TiO_2/C(500), although N dopant moved out from the TiO_2 at the high temperature of 500 °C, *N*-TiO_2/C(500) showed lower band gap energy compared to P25 because oxygen atom vacancies and probably some N dopant were still located on the surface of *N*-TiO_2/C(500). The decrease in the band gap of *N*-TiO_2 suggests the localized nature of nitrogen species in the TiO_2 lattice [49] which occupy some of the oxygen positions in the lattice. The nitrogen doping creates an *N*-induced mid-gap level by hybridization of nitrogen 2p states and oxygen 2p states at the top of the valence band [50], which are responsible for the visible-light absorption. The creation of oxygen vacancies and color centers such as Ti^{3+} also enhances the absorption of visible light [51]. Therefore, the doped nitrogen atoms and oxygen vacancies are involved in the decreasing band gap energy [52].

Photoluminescence

Photoluminescence (PL) test was conducted to reveal the trapping and transfer of charge carriers in the materials. The measured PL emission spectra of the prepared nitrogen doped TiO_2 samples are presented in Fig. 9. The emission intensity of *N*-TiO_2(500) was lower than TiO_2. In addition, the emission spectra of *N*-TiO_2 and *N*-TiO_2/C were the same and their intensities were considerably lower than that of *N*-TiO_2(500). The lower PL intensity explains that *N*-TiO_2 samples efficiently hold the separation of the charge carriers and retard their recombination compared to TiO_2. The lower recombination rate of photogenerated e^--h^+ pairs results in the lower PL emission spectra [53]. The influence of the enhanced charge separation is displayed in their photocatalytic reaction.

Photocatalytic activity

The process of RhB removal on the prepared composites *N*-TiO_2, *N*-TiO_2/C and *N*-TiO_2/C(500) was evaluated under visible light irradiation and the results are shown in Fig. 10. During the reaction, the absorption bands of RhB dye gradually decreased, then its color changed from magenta to green, then yellow, and finally disappeared (Fig. 11); *N*-doped

Fig. 11. Color change of the RhB solution under visible light irradiation and in the presence of *N*-TiO_2/C. Measurement conditions: 40 mg photocatalyst, 40 mL RhB aqueous solution containing 10 ppm of RhB, and a light source of 40-Watt white LED lamp

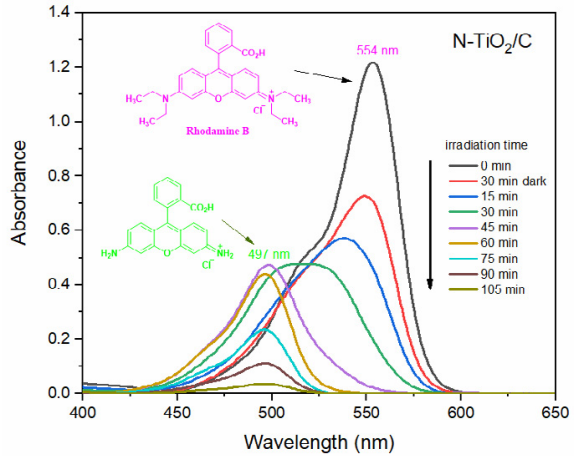

Fig. 12. UV-Vis spectral changes of an RhB solution under visible light irradiation and in the presence of *N*-TiO_2/C.

TiO_2 sample removed 94% of the RhB after 150 min. When modified with 3 wt% biochar, the *N*-TiO_2/C photocatalyst removed with noticeably higher photocatalytic rate, 97% of the RhB in 105 min, suggesting its relatively high adsorption ability towards RhB due to its high surface area, porosity and high surface hydroxyl groups as mentioned before. It is clearly seen that the biochar in *N*-TiO_2/C provides active sites for enhancing the adsorption of RhB. When the calcinated *N*-TiO_2/C was used, the ratio of the removed RhB was only 22% after 180 min, showing the effect of lower specific surface (Table 1). There are also other studies which demonstrate the significant effect of crystallinity and specific surface area on the photocatalytic activity of TiO_2 composites [54]. Considering the appropriate band gap, large specific surface area and good adsorption ability, the *N*-TiO_2/C photocatalyst manifested the best photocatalytic performance for the degradation of RhB among all other samples.

As seen in Fig. 10 and Fig. 12, under visible light and in the presence of *N*-TiO_2 and *N*-TiO_2/C photocatalysts, the maximum absorption peak of RhB shifted gradually from 554 nm to 497 nm, implying that there were different intermediate products. The most probable intermediates for RhB are *N*-de-ethylated species [55]: *N,N,N′*- triethyl rhodamine (maximum peak 537 nm), *N,N′*-diethyl rhodamine (521 nm), *N*-ethyl rhodamine (505 nm), and thoroughly de-ethylated rhodamine (495 nm). Fig. 13 shows the changes of absorbance and wavelength shift for RhB solution maximum peak with time during the photocatalytic process.

The complete de-ethylation and more than 50% degradation of RhB occurred in the first 45 min and 120 min with the photocatalyst *N*-TiO_2/C and *N*-TiO_2, respectively (Fig. 13). The

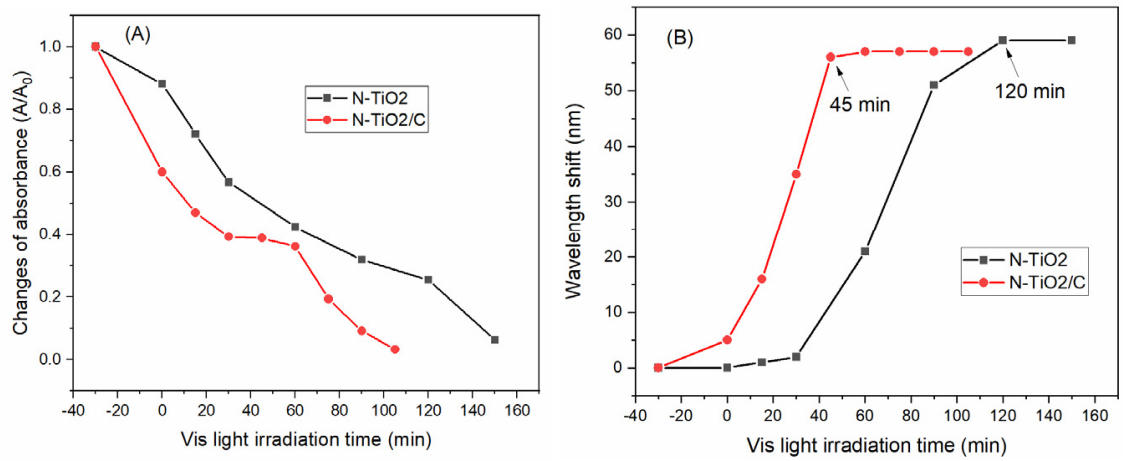

Fig. 13. (A) Absorbance changes and (B) the corresponding wavelength shifts of RhB solution maximum peak with visible-light irradiation time during the photocatalytic processes. In the calculation of absorbance change, for simplicity it was assumed that tetraethyl-rhodamine and its de-ethylated derivatives have the same molar absorptivity

photodegradation of a dye assisted by TiO_2 particles via *N*-de-ethylation occurs only when it is on the semiconductor surface, and not in bulk solution [56]. Since the band gap energy of the prepared *N*-doped TiO_2 materials (about 3 eV) is not low enough for efficient visible light absorption, it is concluded that the adsorbed RhB dye serves as a sensitizer. Under the irradiation by visible light, the adsorbed RhB dye undergoes electronic excitation by absorbing photons at $\lambda > 470$ nm (about 2.6 eV). An excited RhB molecule then injects electrons into the conduction band of the TiO_2 particles and initiates the chemical degradation [11, 12]. Therefore, RhB can undergoe photodegradation through a solution bulk reaction or a surface reaction [57]. The hydroxyl radicals (•OH), formed via the excitation of the electrons from the valence band to the conduction band of TiO_2 under the light irradiation, promote the solution bulk reaction and lead to the photodecomposition of RhB in the aqueous solution. Moreover, the surface reaction is induced when the excited RhB injects electrons to the conduction band of the TiO_2 and generates hydroxyl radicals. The hydroxyl radicals formed via this pathway cause the spontaneous de-ethylation of adsorbed RhB molecules [55], which shift the maximum peak from 554 to 497 nm in the UV-Vis spectrum. However, in the decomposition of RhB molecules via the solution bulk reaction the absorbance of RhB is simply decreased without a peak shift. As shown in Fig. 10 and Fig. 13, the absorbance spectra of the *N*-TiO_2 and *N*-TiO_2/C solutions demonstrate a significant peak shift from $\lambda = 554$ nm to $\lambda = 496$ nm, while no peak shift in the case of the *N*-TiO_2/C(500) solution was observed. These results indicate that the surface reaction rates for *N*-TiO_2 and *N*-TiO_2/C were much larger than that obtained for *N*-TiO_2/C(500). In fact, no surface reaction occurs on *N*-TiO_2/C(500) photocatalyst (Fig. 10); the surface reaction rate on *N*-TiO_2/C is higher than that of *N*-TiO_2.

The high activity and desirable properties of our synthesized *N*-TiO_2/C nanocomposite in terms of low amount of catalyst used and the power light, is clearly seen in comparison with the earlier reported doped TiO_2 (Table 2).

In summary, during the process of RhB removal on the *N*-TiO_2/C surface, the biochar enhances the surface adsorption of RhB on the photocatalyst, which causes an increase in surface reaction rate and a concentration effect for photodegrading RhB. The higher photocatalytic activity of *N*-TiO_2/C with respect to *N*-TiO_2 is mainly attributed to its higher surface adsorption of RhB, 40 wt% and 10 wt% in 30 min by *N*-TiO_2/C and *N*-TiO_2, respectively (Fig. 13). Additionally, the visible light absorbance of *N*-TiO_2/C is higher than that of *N*-TiO_2 due to its lower band gap energy and the presence of the modified biochar. UV-Vis spectra of *N*-TiO_2/C solution reveal that the absorbance at 497 nm decreased dramatically within 60 min after the 45 min initial rapid surface reaction. These findings show that *N*-TiO_2/C efficiently decomposed RhB under visible light irradiation via both the fast surface reaction and the solution bulk reaction. It appeared that the biochar is an efficient promoter

Table 2. Comparison of the catalytic activity of the *N*-TiO_2/C with other documented doped TiO_2 catalysts in the degradation of RhB under visible light

photocatalyst	Reaction condition	highlights	Ref.
N-TiO_2/C	40 mg catalyst, 40 mL of 10 ppm RhB, 40 W white LED lamp	100% degradation after 105 min	This work
N- and *S*-codoped TiO_2	60 mg NSTs, 150 mL RhB 10 ppm, 400 W halogen spotlight	100% degradation after 120 min	[14]
C-, S-, N-, and Fe-doped TiO_2	30 mg catalyst 100 mL of 5 ppm RhB, 1000 W high-pressure Hg arc lamp	rate constant 0.0029 min^{-1} for CNS-0.5 Fe-TiO_2	[58]
C and *N* co-doped TiO_2	400 mg catalyst, 200 mL of 50 ppm RhB Ultrasonic irradiation frequency of 35 kHz, 50 W	rate constant of 0.0226 min^{-1}	[59]
C and *N* codoped TiO_2	180 mg catalyst, 100 mL of 5 ppm RhB a 36 W compact fluorescent lamp	100 % degradation after 180 min rate constant 0.0427 min^{-1}	[60]

that facilitates *N*-TiO_2/C nanocomposite in driving effectively the photochemical degradation reactions by adjusting three main limitations of pure TiO_2: inducing the absorbance of a higher amount of photoenergy in the visible region, enhancing the RhB dye adsorption, and assisting the effective separation of the photocatalytically produced electron-hole. This study offers the use of abundant and sustainable resources via an economical method to harness the usage of solar energy for wastewater treatment in the future.

CONCLUSION

Three materials of nitrogen-doped TiO_2 including *N*-TiO_2/C (modified with biochar), calcinated *N*-TiO_2/C at 500 °C, and *N*-TiO_2 were successfully synthesized by a simple one-step sol-gel method. As prepared *N*-doped TiO_2 materials uncovered improved interesting properties compared to pure TiO_2. The highest photocatalytic activity for the degradation of RhB dye in the visible region was obtained for *N*-TiO_2/C nanocomposite (100% removal in 105 min), due to its favorable properties such as the highest mesoporous surface area and porosity, surface hydroxyls, and the lowest band gap energy. *N*-TiO_2/C nanocomposite could decompose RhB through both dye-sensitization and photocatalytic pathways. It appeared that the widely available biochar is an efficient promoter that helps *N*-TiO_2/C nanocomposite in driving effectively the photochemical degradation reactions by adjusting three primary limitations of pure TiO_2: inducing the absorbance of a higher amount of photoenergy in the visible domain, enhancing the RhB dye adsorption, and assisting the effective separation of the photocatalytically produced electron-hole.

ACKNOWLEDGEMENTS

The authors are grateful for the financial support of this study by the University of Zanjan, Amirkabir University of Technology and the Iran National Science Foundation under Grant No. INSF 97009020.

DECLARATION OF COMPETING INTERESTS

The authors declare that they have no known competing financial interests or personal relationships that could have appeared to influence the work reported in this paper.

REFERENCES

1. Zhao X, Zhang X, Zhao B, Jia F, Han D, Fan Y, et al. A direct oxygen vacancy essential Z-scheme C@Ti4O7/g-C3N4 heterojunctions for visible-light degradation towards environmental dye pollutants. Applied Surface Science. 2020;525:146486.
2. Izumi I, Fan F-RF, Bard AJ. Heterogeneous photocatalytic decomposition of benzoic acid and adipic acid on platinized titanium dioxide powder. The photo-Kolbe decarboxylative route to the breakdown of the benzene ring and to the production of butane. The Journal of Physical Chemistry. 1981;85(3):218-23.
3. Konstantinou IK, Albanis TA. TiO2-assisted photocatalytic degradation of azo dyes in aqueous solution: kinetic and mechanistic investigations. Applied Catalysis B: Environmental. 2004;49(1):1-14.
4. Zhang P, Zhang J, Gong J. Tantalum-based semiconductors for solar water splitting. Chem Soc Rev. 2014;43(13):4395-422.
5. Di Paola A, García-López E, Marcì G, Palmisano L. A survey of photocatalytic materials for environmental remediation. Journal of Hazardous Materials. 2012;211-212:3-29.
6. Dozzi MV, Selli E. Doping TiO2 with p-block elements: Ef-

fects on photocatalytic activity. Journal of Photochemistry and Photobiology C: Photochemistry Reviews. 2013;14:13-28.
7. Shaik SA, Goswami A, Varma RS, Gawande MB. Nitrogen-doped nanocarbons (NNCs): Current status and future opportunities. Current Opinion in Green and Sustainable Chemistry. 2019;15:67-76.
8. Pelaez M, Baruwati B, Varma RS, Luque R, Dionysiou DD. Microcystin-LR removal from aqueous solutions using a magnetically separable N-doped TiO2 nanocomposite under visible light irradiation. Chemical Communications. 2013;49(86):10118.
9. Zheng Z, Zhao J, Yuan Y, Liu H, Yang D, Sarina S, et al. Tuning the Surface Structure of Nitrogen-Doped TiO2Nanofibres-An Effective Method to Enhance Photocatalytic Activities of Visible-Light-Driven Green Synthesis and Degradation. Chemistry - A European Journal. 2013;19(18):5731-41.
10. Sakthivel S, Janczarek M, Kisch H. Visible Light Activity and Photoelectrochemical Properties of Nitrogen-Doped TiO2. The Journal of Physical Chemistry B. 2004;108(50):19384-7.
11. Vinodgopal K, Kamat PV. Photochemistry on surfaces: photodegradation of 1,3-diphenylisobenzofuran over metal oxide particles. The Journal of Physical Chemistry. 1992;96(12):5053-9.
12. Zhang F, Zhao J, Zang L, Shen T, Hidaka H, Pelizzetti E, et al. Photoassisted degradation of dye pollutants in aqueous TiO2 dispersions under irradiation by visible light. Journal of Molecular Catalysis A: Chemical. 1997;120(1-3):173-8.
13. Takizawa T, Watanabe T, Honda K. Photocatalysis through excitation of adsorbates. 2. A comparative study of Rhodamine B and methylene blue on cadmium sulfide. The Journal of Physical Chemistry. 1978;82(12):1391-6.
14. Chung J, Chung JW, Kwak S-Y. Adsorption-assisted photocatalytic activity of nitrogen and sulfur codoped TiO2 under visible light irradiation. Physical Chemistry Chemical Physics. 2015;17(26):17279-87.
15. Jia F, Yao Z, Jiang Z, Li C. Preparation of carbon coated TiO2 nanotubes film and its catalytic application for H2 generation. Catalysis Communications. 2011;12(6):497-501.
16. Ząbek P, Eberl J, Kisch H. On the origin of visible light activity in carbon-modified titania. Photochemical & Photobiological Sciences. 2009;8(2):264.
17. Zhao L, Chen X, Wang X, Zhang Y, Wei W, Sun Y, et al. One-Step Solvothermal Synthesis of a Carbon@TiO2 Dyade Structure Effectively Promoting Visible-Light Photocatalysis. Advanced Materials. 2010;22(30):3317-21.
18. Zheng H, Wang Z, Zhao J, Herbert S, Xing B. Sorption of antibiotic sulfamethoxazole varies with biochars produced at different temperatures. Environmental Pollution. 2013;181:60-7.
19. Tan X-f, Liu Y-g, Gu Y-l, Xu Y, Zeng G-m, Hu X-j, et al. Biochar-based nano-composites for the decontamination of wastewater: A review. Bioresource Technology. 2016;212:318-33.
20. Xie M, Chen W, Xu Z, Zheng S, Zhu D. Adsorption of sulfonamides to demineralized pine wood biochars prepared under different thermochemical conditions. Environmental Pollution. 2014;186:187-94.
21. Cai X, Li J, Liu Y, Yan Z, Tan X, Liu S, et al. Titanium dioxide-coated biochar composites as adsorptive and photocatalytic degradation materials for the removal of aqueous organic pollutants. Journal of Chemical Technology & Biotechnology. 2017;93(3):783-91.
22. Zhang H, Wang Z, Li R, Guo J, Li Y, Zhu J, et al. TiO2 supported on reed straw biochar as an adsorptive and photocatalytic composite for the efficient degradation of sulfamethoxazole in aqueous matrices. Chemosphere. 2017;185:351-60.
23. Kim JR, Kan E. Heterogeneous photocatalytic degradation of sulfamethoxazole in water using a biochar-supported TiO2 photocatalyst. Journal of Environmental Management. 2016;180:94-101.
24. Saadoun L, Ayllón JA, Jiménez-Becerril J, Peral J, Domènech X, Rodríguez-Clemente R. 1,2-Diolates of titanium as suitable precursors for the preparation of photoactive high surface titania. Applied Catalysis B: Environmental. 1999;21(4):269-77.
25. Langford JI, Wilson AJC. Scherrer after sixty years: A survey and some new results in the determination of crystallite size. Journal of Applied Crystallography. 1978;11(2):102-13.
26. López R, Gómez R. Band-gap energy estimation from diffuse reflectance measurements on sol–gel and commercial TiO2: a comparative study. Journal of Sol-Gel Science and Technology. 2011;61(1):1-7.
27. Barka N, Qourzal S, Assabbane A, Nounah A, Ait-Ichou Y. Factors influencing the photocatalytic degradation of Rhodamine B by TiO2-coated non-woven paper. Journal of Photochemistry and Photobiology A: Chemistry. 2008;195(2-3):346-51.
28. Niederberger M, Garnweitner G, Krumeich F, Nesper R, Cölfen H, Antonietti M. Tailoring the Surface and Solubility Properties of Nanocrystalline Titania by a Nonaqueous In Situ Functionalization Process. Chemistry of Materials. 2004;16(7):1202-8.
29. Khan SUM. Efficient Photochemical Water Splitting by a Chemically Modified n-TiO2. Science. 2002;297(5590):2243-5.
30. Gregg S SK. Adsorption, surface area and porosity. London Academic Press; 1982.
31. Sing KSW. Reporting physisorption data for gas/solid systems with special reference to the determination of surface area and porosity (Recommendations 1984). Pure and Applied Chemistry. 1985;57(4):603-19.
32. Galarneau A, Mehlhorn D, Guenneau F, Coasne B, Villemot F, Minoux D, et al. Specific Surface Area Determination for Microporous/Mesoporous Materials: The Case of Mesoporous FAU-Y Zeolites. Langmuir. 2018;34(47):14134-42.
33. Xu P, Lu J, Xu T, Gao S, Huang B, Dai Y. I2-Hydrosol-Seeded Growth of (I2)n-C-Codoped Meso/Nanoporous TiO2 for Visible Light-Driven Photocatalysis. The Journal of Physical Chemistry C. 2010;114(20):9510-7.
34. Wang A, Yu W, Fang Y, Song Y, Jia D, Long L, et al. Facile hydrothermal synthesis and optical limiting properties of TiO 2 -reduced graphene oxide nanocomposites. Carbon. 2015;89:130-41.
35. Litke A, Su Y, Tranca I, Weber T, Hensen EJM, Hofmann JP. Role of Adsorbed Water on Charge Carrier Dynamics in Photoexcited TiO2. The Journal of Physical Chemistry C. 2017;121(13):7514-24.
36. Pori P, Vilčnik A, Petrič M, Sever Škapin A, Mihelčič M, Šurca Vuk A, et al. Structural studies of TiO 2 /wood coatings prepared by hydrothermal deposition of rutile particles from TiCl 4 aqueous solutions on spruce (Picea Abies) wood. Applied Surface Science. 2016;372:125-38.
37. Pan L, Zou J-J, Zhang X, Wang L. Water-Mediated Promotion

of Dye Sensitization of TiO2 under Visible Light. Journal of the American Chemical Society. 2011;133(26):10000-2.
38. Morgan BJ, Watson GW. A Density Functional Theory + U Study of Oxygen Vacancy Formation at the (110), (100), (101), and (001) Surfaces of Rutile TiO2. The Journal of Physical Chemistry C. 2009;113(17):7322-8.
39. Ghosh AK, Wakim FG, Addiss RR. Photoelectronic Processes in Rutile. Physical Review. 1969;184(3):979-88.
40. Pan X, Yang M-Q, Fu X, Zhang N, Xu Y-J. Defective TiO2 with oxygen vacancies: synthesis, properties and photocatalytic applications. Nanoscale. 2013;5(9):3601.
41. Erjavec B, Kaplan R, Pintar A. Effects of heat and peroxide treatment on photocatalytic activity of titanate nanotubes. Catalysis Today. 2015;241:15-24.
42. Colmenares JC, Varma RS, Lisowski P. Sustainable hybrid photocatalysts: titania immobilized on carbon materials derived from renewable and biodegradable resources. Green Chemistry. 2016;18(21):5736-50.
43. Peng T, Zhao D, Dai K, Shi W, Hirao K. Synthesis of Titanium Dioxide Nanoparticles with Mesoporous Anatase Wall and High Photocatalytic Activity. The Journal of Physical Chemistry B. 2005;109(11):4947-52.
44. Anpo M, Aikawa N, Kubokawa Y, Che M, Louis C, Giamello E. Photoluminescence and photocatalytic activity of highly dispersed titanium oxide anchored onto porous Vycor glass. The Journal of Physical Chemistry. 1985;89(23):5017-21.
45. Etacheri V, Seery MK, Hinder SJ, Pillai SC. Highly Visible Light Active TiO2−xNx Heterojunction Photocatalysts. Chemistry of Materials. 2010;22(13):3843-53.
46. Wang X, Wang X, Zhao J, Chen J, Zhang J, Song J, et al. Bioframe synthesis of NF–TiO2/straw charcoal composites for enhanced adsorption-visible light photocatalytic degradation of RhB. RSC Advances. 2015;5(82):66611-20.
47. Jia L, Wang D-H, Huang Y-X, Xu A-W, Yu H-Q. Highly Durable N-Doped Graphene/CdS Nanocomposites with Enhanced Photocatalytic Hydrogen Evolution from Water under Visible Light Irradiation. The Journal of Physical Chemistry C. 2011;115(23):11466-73.
48. Chen C, Cai W, Long M, Zhou B, Wu Y, Wu D, et al. Synthesis of Visible-Light Responsive Graphene Oxide/TiO2 Composites with p/n Heterojunction. ACS Nano. 2010;4(11):6425-32.
49. Sathish M, Viswanathan B, Viswanath RP, Gopinath CS. Synthesis, Characterization, Electronic Structure, and Photocatalytic Activity of Nitrogen-Doped TiO2 Nanocatalyst. Chemistry of Materials. 2005;17(25):6349-53.
50. Umebayashi T, Yamaki T, Yamamoto S, Miyashita A, Tanaka S, Sumita T, et al. Sulfur-doping of rutile-titanium dioxide by ion implantation: Photocurrent spectroscopy and first-principles band calculation studies. Journal of Applied Physics. 2003;93(9):5156-60.
51. Serpone N. Is the Band Gap of Pristine TiO2Narrowed by Anion- and Cation-Doping of Titanium Dioxide in Second-Generation Photocatalysts? The Journal of Physical Chemistry B. 2006;110(48):24287-93.
52. Yang G, Jiang Z, Shi H, Xiao T, Yan Z. Preparation of highly visible-light active N-doped TiO2 photocatalyst. Journal of Materials Chemistry. 2010;20(25):5301.
53. Han C, Zhang N, Xu Y-J. Structural diversity of graphene materials and their multifarious roles in heterogeneous photocatalysis. Nano Today. 2016;11(3):351-72.
54. Muñoz-Batista MJ, Kubacka A, Fernández-García M. Effective Enhancement of TiO2 Photocatalysis by Synergistic Interaction of Surface Species: From Promoters to Co-catalysts. ACS Catalysis. 2014;4(12):4277-88.
55. Watanabe T, Takizawa T, Honda K. Photocatalysis through excitation of adsorbates. 1. Highly efficient N-deethylation of rhodamine B adsorbed to cadmium sulfide. The Journal of Physical Chemistry. 1977;81(19):1845-51.
56. Zhang F, Zhao J, Shen T, Hidaka H, Pelizzetti E, Serpone N. TiO2-assisted photodegradation of dye pollutants II. Adsorption and degradation kinetics of eosin in TiO2 dispersions under visible light irradiation. Applied Catalysis B: Environmental. 1998;15(1-2):147-56.
57. Wu T, Liu G, Zhao J, Hidaka H, Serpone N. Photoassisted Degradation of Dye Pollutants. V. Self-Photosensitized Oxidative Transformation of Rhodamine B under Visible Light Irradiation in Aqueous TiO2 Dispersions. The Journal of Physical Chemistry B. 1998;102(30):5845-51.
58. Yang X, Cao C, Erickson L, Hohn K, Maghirang R, Klabunde K. Photo-catalytic degradation of Rhodamine B on C-, S-, N-, and Fe-doped TiO2 under visible-light irradiation. Applied Catalysis B: Environmental. 2009;91(3-4):657-62.
59. Pang YL, Abdullah AZ. Effect of carbon and nitrogen co-doping on characteristics and sonocatalytic activity of TiO2 nanotubes catalyst for degradation of Rhodamine B in water. Chemical Engineering Journal. 2013;214:129-38.
60. Le TTT, Tran TD. Photocatalytic Degradation of Rhodamine B by C and N Codoped TiO2 Nanoparticles under Visible-Light Irradiation. Journal of Chemistry. 2020;2020:1-8.